



# Flow-Driven Deformation in Granular Porous Media: Dimensionless Analysis

Min-Kyung Jeon<sup>1</sup> · Seunghee Kim<sup>2</sup> · Tae-Hyuk Kwon<sup>3</sup>

Received: 4 October 2023 / Accepted: 26 April 2024 / Published online: 20 May 2024  
© The Author(s) 2024

## Abstract

Fluid injection can induce mechanical deformation in granular porous media due to the elevation of internal pore fluid pressure. This gains more significance when more than two immiscible fluids are involved, attributable to capillary and viscous drag forces. Such a coupled hydromechanical behavior associated with immiscible fluid flows plays an important role in injection, storage, and recovery of fluids in deformable porous media. This study presents a dimensionless map with newly proposed dimensionless parameters to predict deformation occurrence due to an immiscible fluid flow in deformable porous media. A series of hydromechanically coupled pore network simulations are first performed while varying the capillary number, mobility ratio, medium stiffness, and effective confining stress over orders of magnitudes. The compilation of simulation results with previously published Hele–Shaw experiment results is analyzed with the dimensionless parameters, such as the capillary number, mobility ratio, particle-level force ratios, and particle-level pressure ratios. Particularly, the particle-level pressure ratios include the capillary pressure ratio, defined as the ratio of capillary pressure to fracture pressure, and the viscous drag pressure, defined as the ratio of viscous drag pressure to fracture pressure. The dimensionless map based on the particle-level pressure ratios, where the capillary pressure ratio and viscous drag pressure ratio are defined as the ratios of capillary pressure and viscous drag pressure to fracture pressure, effectively delineates four deformation regimes—no deformation, capillary-induced deformation, drag-driven deformation, and mixed-mode deformation. The results demonstrate that capillary-induced deformation occurs when the capillary pressure ratio is greater than  $10^{-1}$ , while drag-driven deformation is observed when the viscous drag pressure ratio exceeds  $10^{-2}$ . The presented dimensionless map and dimensionless parameters are expected to be applicable for geological subsurface processes, including geological storage of carbon dioxide and hydrogen, and enhanced oil recovery.

## Article Highlights

- Hydromechanically coupled PNM examines hydromechanical responses of granular porous media subjected to immiscible fluid flows.
- A dimensionless map with capillary and viscous pressure ratios effectively captures flow-driven deformation in deformable porous media.

- The dimensionless map is applicable for practices involving injection, storage, and recovery of fluids in deformable porous media.

**Keywords** Dimensionless analysis · Deformable granular media · Two-phase flow · Hydromechanical behavior · Pore network model

### Abbreviations

$a$	Radius of particle
$r$	Throat radius
$\lambda$	Disorder coefficient of pore network
$K$	Spring stiffness
$E^*$	Effective elastic modulus of grains
$E$	Medium stiffness ( $E = K/(2 \cdot a) = E^* \sqrt{h/(2 \cdot a)}$ )
$h$	Spring contraction
$h_o$	Initial spring contraction
$\mu_{in}$	Viscosity of the invading fluid
$\mu'$	Apparent viscosity of granular medium
$M$	Mobility ratio
Ca	Capillary number
$Q$	Flow rate
$V$	Flow velocity
$\gamma$	Interfacial tension
$\sigma'$	Effective confining stress
RMSD	Root mean-squared displacement
$F_v$	Viscous seepage force ( $6\pi\mu aV$ )
$F_c$	Capillary force ( $F_c = \pi a \gamma$ )
$F_{sk}$	Skeletal force ( $F_{sk} = 4a^2 \sigma'$ )
$t_d$	Diffusion time scale ( $t_d = \mu l^2 / E/k$ )
$t_i$	Injection time scale ( $t_i = l/V$ )
$l$	Characteristic length of injection process or crack tip length ( $l = 2a$ )
$t_r$	Retardation time scale ( $t_r = \mu'/E$ )
$N_f$	Fracturing number, $N_f = \frac{\sqrt{2\gamma}}{\lambda E^* (ah)^{\frac{1}{2}}}$
Ca*	Modified capillary number ( $Ca^* = Ca \frac{l}{2a} \chi^{-1}(\lambda)$ , where $\chi(\lambda) = \frac{\lambda}{(1-\lambda^2)}$ )
$L$	Macroscopic length scale ( $L = 2 \cdot a \cdot n$ )
$P_{frac}$	Fracture pressure, $P_{frac} = \sqrt{\gamma E/l} +  \sigma'_0 $
$P_c$	Capillary pressure ( $P_c = 2\gamma/r$ )
$P_v$	Viscous drag pressure ( $P_v = 6\mu V/a$ )

## 1 Introduction

The injection of a fluid into porous media can alter pore fluid pressure and cause deformations and fractures in the host media. Such a poromechanical phenomenon plays an essential role across a wide range of scales from geological subsurface processes including geologic carbon storage, geothermal energy extraction, enhanced oil recovery,

and hydraulic fracturing, to biological practices such as fluid transport through living cells and tissues, and to energy applications such as fuel cells (Atrazhev et al. 2013; Budday et al. 2015; Franceschini et al. 2006; Gutierrez et al. 2015; Monfared and Rothenburg 2016; Støverud et al. 2012). Especially, alteration in permeability of porous media by deformation has a significant effect on the efficiency of fluid recovery and storage in subsurface geologic formations, as well as in soft porous media such as biological tissues (Budday et al. 2015; Franceschini et al. 2006; Gutierrez et al. 2015; Monfared and Rothenburg 2016; Støverud et al. 2012).

Interplays between fluid flows and mechanical deformation in granular media and ensuing fluid-driven opening and fractures have been examined in a variety of conditions, mostly through Hele–Shaw cell experiments (Choi et al. 2011; Huang et al. 2012; Jeon et al. 2020a, b; Lee et al. 2020; MacMinn et al. 2015; Rocco et al. 2017; Sandnes et al. 2011; Shin and Santamarina 2010; Sun and Santamarina 2019; Zadeh et al. 2023) and by using numerical modeling (Carrillo et al. 2020; Carrillo and Bourg 2021a, b; Cho et al. 2019; Holtzman and Juanes 2010; Jain and Juanes 2009; Jeon et al. 2020a; MacMinn et al. 2015; Mahabadi and Jang 2017; Meng et al. 2020). In compacted granular media, parameters such as particle size, boundary stress, medium stiffness, medium disorder, interfacial tension, fluid viscosity, and flow rate determine the flow regime and host media behavior from pore invasion including fingering and stable displacement to fracturing. Previous studies reveal that the hydromechanical behavior can be explained by the dominant forces in the system, including inertia, viscous drag, capillarity, and friction (*e.g.*, Choi et al. 2011; Holtzman and Juanes 2010; Shin and Santamarina 2010; Sandnes et al. 2011). Accordingly, the dimensionless analysis has followed to compare the relevant forces acting on the system and assess the hydromechanical behavior of granular media. Various conceptual maps based on dimensionless parameters such as capillary number, fracturing number, characteristic time ratios, force ratios, and pressure ratios have been proposed to elucidate flow patterns and hydraulic fracturing regimes (*e.g.*, Holtzman and Juanes 2010; Shin and Santamarina 2010; Huang et al. 2012; Jeon et al. 2020a). Recently, Carrillo and Bourg (2021a) and Zadeh et al. (2023) have delved into dimensionless analyses of the deformation induced by viscous flow in soft granular materials through continuum modeling and Hele–Shaw cell experiments. Despite these efforts, quantitative boundaries still remain elusive, and there is still a lack of comprehensive evaluation for the proposed dimensionless parameters, coupled with a scarcity of both experimental and numerical data at this junction. Particularly, the dimensionless parameters used in the literature hardly capture the effect of grain stiffness and/or medium stiffness because experimental or numerical data on two-phase flows in soft deformable porous media are very scarce. Moreover, the majority of the data to date are limited to the cases in stiff media either with inviscible gas or miscible viscous fluid, leaving a knowledge gap on the fluid-driven deformation in soft deformable porous media.

In this regard, this study explores the deformation caused by immiscible fluid flows in deformable porous media through a numerical approach using a hydromechanically coupled pore network model (HM-PNM) and suggests a dimensionless map to predict the occurrence of fluid-driven deformations. To begin, a series of simulations using the HM-PNM was conducted. This involved injecting an immiscible fluid into fluid-saturated granular porous media while systematically varying parameters such as fluid viscosity, injection flow rate, and interfacial tension. The scope of the HM-PNM simulations encompassed diverse values of input and boundary conditions, which covered a wide range of the capillary number, mobility ratio, medium stiffness, and effective confining stress spanning several orders of magnitude. The relations among various dimensionless

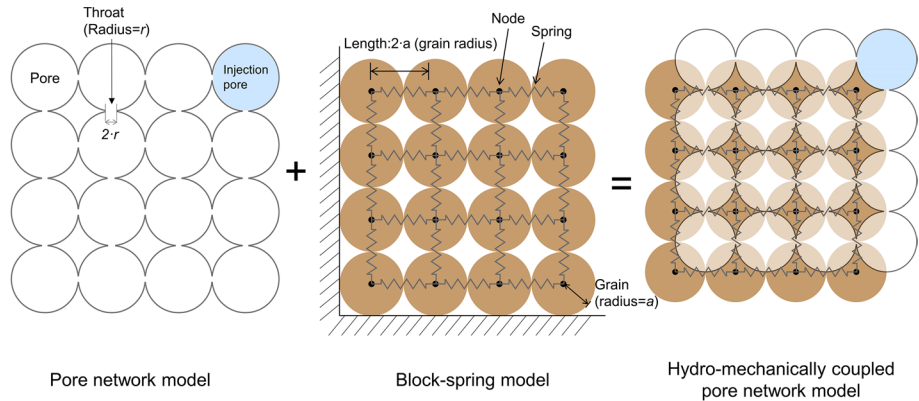


**Fig. 1** A schematic diagram of the hydromechanically coupled pore network model

parameters, such as the capillary number, mobility ratio, particle-level force ratios, and particle-level pressure ratios were then examined by using the simulation outcomes as well as previously published Hele–Shaw experiment results. Finally, a dimensionless map was proposed, highlighting the most elucidating dimensionless parameters. This map serves to define the deformation occurrence caused by the flow of immiscible fluids in soft deformable porous media, which takes into account factors such as medium stiffness and viscosities of the involved fluids.

## 2 Parametric Study Using Hydromechanically Coupled Pore Network Model (HM-PNM) Simulation

### 2.1 Model Description

The numerical modeling provides an advantage over the physical modeling in covering a wide range of test variables, including but not limited to, fluid viscosity, flow rate, medium stiffness, and interfacial tension. This study adopts the quasi-two-dimensional hydromechanically coupled pore network model (HM-PNM) previously developed by Jeon et al. (2020a, b). The earlier version of HM-PNM was capable of simulation of hydromechanical interactions during flows of inviscid and viscous fluids in fluid-saturated deformable porous media (Holtzman and Juanes 2010; Jeon et al. 2020a). The HM-PNM by Jeon et al. (2020a, b) was extended further and modified to simulate deformation by immiscible fluid injection in this study. The extended HM-PNM emulates a pack of spherical solid particles with a radius of  $a$  in a square lattice array, as shown in Fig. 1. The fluid flow in pores is described with pores and throats (*i.e.*, pore network model). The mechanical behavior of the solid sphere pack is represented by nodes and springs (*i.e.*, block-spring model).

The pore network is composed of pores and throats (Fig. 1). The pores have volumes ( $\text{vol}=(8-4/3\pi)\cdot a^2$ ), and they are connected by the throats. Each throat radius,  $r$ , is randomly determined to follow a uniform distribution, representing the inherent heterogeneity of porous media. The average radius of the throats  $r$  is  $a/2$ , and the throat radius distribution is determined using the disorder coefficient  $\lambda \in (0,1)$ , *i.e.*, each throat radius  $r$  has a value between  $(1-\lambda)a/2$  and  $(1+\lambda)a/2$ . A two-phase flow simulation is

conducted by following Stokes' law and the Young–Laplace equation. In the same manner as previous PNM studies, the PNM simulates piston-like immiscible fluid invasion, which occurs when the pressure difference between two adjacent pores exceeds the capillary pressure of the throat connecting the pores (Aker et al. 1998; Al-Gharbi and Blunt 2005; Li et al. 2017).

The skeletal structure of the granular porous media is represented by the simple cubic packing of spherical particles (Fig. 1), which is described with the nodes and the springs connecting the nodes. The mechanical response is governed by the spring response which is described by using the sphere-to-sphere Hertzian contact model. The spring has a nonlinear stiffness, following the Hertzian contact model:

$$K = 2E^* \sqrt{ah/2}, \quad (1)$$

where  $K$  is the spring stiffness,  $E^*$  is the effective elastic modulus of grains, and  $h$  is the spring contraction. Herein, the particles have a uniform radius  $a$ . A boundary force is applied to produce the initial contraction of the springs,  $h_o$ , as an initial condition. The dominant forces exerted on each particle are the force by pore fluid pressure and the contact force between particles. Once the force equilibrium at each node is established, the injection-induced pore pressure change leads to the change of contact force, resulting in particle deformation. Particle rearrangement by deformation modifies the pore size, affecting flow characteristics like capillary pressure or hydraulic conductance (Holtzman and Juanes 2010; Jeon et al. 2020a). Ultimately, a two-way hydromechanical coupling can be conducted during fluid flows. A more detailed explanation of the HM-PNM and its algorithm can be found in Jeon et al. (2020a, b). This study employed a quarter domain, exploiting the symmetric behavior, to reduce the computational workload. The pore at the upper right corner was chosen as the injection pore, in which the fluid injection was imposed for a given flow rate. The pores on the left and bottom edges were designated as outlet pores, and their pressure was set to zero, assumed to be open boundaries. The positions of the particles at the left and bottom boundaries were fixed.

## 2.2 Parametric Simulation Study

A variety of invasion patterns can appear when an immiscible fluid invades into a granular medium saturated with another fluid. This invasion pattern is affected by various factors such as capillary number and mobility ratio associated with fluid characteristics and flows (Aker et al. 1998; Chang et al. 2019; Culligan et al. 2006; Kueper et al. 1989; Lenormand et al. 1988; Zhang et al. 2011; Zheng et al. 2017). Furthermore, deformation behaviors are mainly governed by the mechanical stiffness of a porous medium and the applied effective confining stress as a boundary condition (Sun and Santamarina 2019). Therefore, the parametric study by using the developed HM-PNM simulations was designed to cover a wide range of the capillary number, mobility ratio, medium stiffness, and effective confining stress over orders of magnitudes. The primary parameters include the fluid injection rate, viscosity of the invading fluid, interfacial tension, effective grain modulus, and effective boundary stress. This study modeled a  $50 \times 50$  network with a disorder coefficient  $\lambda$  of 0.3, the particle radius  $a$  of 1 mm, and the average throat radius  $r$  of 0.5 mm. The effective grain modulus varied from 500 kPa to 50 MPa, and the effective confining stress from 2.5 to 250 kPa, respectively. The porous medium was assumed to be saturated with water prior to the injection of an immiscible fluid. Upon the force equilibrium at all nodes, an

**Table 1** Input parameters and dimensionless numbers for parametric studies

Case #	$\gamma$ (mN/m)	$\mu_{in}$ (mPa·s)	$Q$ (m <sup>3</sup> /s)	$E^*$ (kPa)	$\sigma'$ (kPa)	$F_s/F_{sk}$	$F_c/F_{sk}$	$P_c/P_{frac}$	$P_v/P_{frac}$
S1	5	0.01	10 <sup>-6</sup>	500	25	6.00 × 10 <sup>-7</sup>	1.57 × 10 <sup>-4</sup>	7.52 × 10 <sup>-4</sup>	7.19 × 10 <sup>-7</sup>
S2	5	1	10 <sup>-6</sup>	500	25	6.00 × 10 <sup>-5</sup>	1.57 × 10 <sup>-4</sup>	7.52 × 10 <sup>-4</sup>	7.19 × 10 <sup>-5</sup>
S3	5	28	10 <sup>-6</sup>	500	25	1.68 × 10 <sup>-3</sup>	1.57 × 10 <sup>-4</sup>	7.52 × 10 <sup>-4</sup>	2.01 × 10 <sup>-3</sup>
S4	5	0.01	10 <sup>-6</sup>	1000	2.5	6.00 × 10 <sup>-6</sup>	1.57 × 10 <sup>-3</sup>	4.22 × 10 <sup>-3</sup>	4.03 × 10 <sup>-6</sup>
S5	5	0.01	10 <sup>-5</sup>	1000	2.5	6.00 × 10 <sup>-5</sup>	1.57 × 10 <sup>-3</sup>	4.22 × 10 <sup>-3</sup>	4.03 × 10 <sup>-5</sup>
S6	5	0.01	10 <sup>-4</sup>	1000	2.5	6.00 × 10 <sup>-4</sup>	1.57 × 10 <sup>-3</sup>	4.22 × 10 <sup>-3</sup>	4.03 × 10 <sup>-4</sup>
S7	5	28	10 <sup>-8</sup>	500	25	1.68 × 10 <sup>-5</sup>	1.57 × 10 <sup>-4</sup>	7.52 × 10 <sup>-4</sup>	2.01 × 10 <sup>-5</sup>
S8	5	28	10 <sup>-4</sup>	500	25	1.68 × 10 <sup>-1</sup>	1.57 × 10 <sup>-4</sup>	7.52 × 10 <sup>-4</sup>	2.01 × 10 <sup>-1</sup>
S9	45	0.01	10 <sup>-6</sup>	500	25	6.00 × 10 <sup>-7</sup>	1.41 × 10 <sup>-3</sup>	6.05 × 10 <sup>-3</sup>	6.42 × 10 <sup>-7</sup>
S10	100	0.01	10 <sup>-6</sup>	500	25	6.00 × 10 <sup>-7</sup>	3.14 × 10 <sup>-3</sup>	1.25 × 10 <sup>-2</sup>	5.96 × 10 <sup>-7</sup>
S11	45	28	10 <sup>-6</sup>	500	25	1.68 × 10 <sup>-3</sup>	1.41 × 10 <sup>-3</sup>	6.05 × 10 <sup>-3</sup>	1.80 × 10 <sup>-3</sup>
S12	100	28	10 <sup>-6</sup>	500	25	1.68 × 10 <sup>-3</sup>	3.14 × 10 <sup>-3</sup>	1.25 × 10 <sup>-2</sup>	1.67 × 10 <sup>-3</sup>
S13	45	28	10 <sup>-12</sup>	500	3.75	1.12 × 10 <sup>-8</sup>	9.42 × 10 <sup>-3</sup>	2.12 × 10 <sup>-2</sup>	6.30 × 10 <sup>-9</sup>
S14	45	28	10 <sup>-12</sup>	5000	3.75	1.12 × 10 <sup>-8</sup>	9.42 × 10 <sup>-3</sup>	9.60 × 10 <sup>-3</sup>	2.85 × 10 <sup>-9</sup>
S15	45	28	10 <sup>-12</sup>	50,000	3.75	1.12 × 10 <sup>-8</sup>	9.42 × 10 <sup>-3</sup>	3.52 × 10 <sup>-3</sup>	1.04 × 10 <sup>-9</sup>
S16	45	28	10 <sup>-6</sup>	500	0.25	1.68 × 10 <sup>-1</sup>	1.41 × 10 <sup>-1</sup>	3.60 × 10 <sup>-2</sup>	1.07 × 10 <sup>-2</sup>
S17	45	28	10 <sup>-6</sup>	500	2.5	1.68 × 10 <sup>-2</sup>	1.41 × 10 <sup>-2</sup>	2.49 × 10 <sup>-2</sup>	7.38 × 10 <sup>-3</sup>

immiscible fluid was injected into water-saturated deformable porous media at a constant flow rate, in which the viscosity of an invading fluid varied from 0.01 to 28 mPa·s, the interfacial tension from 5 to 100 mN/m, and the injection rate from 10<sup>-12</sup> to 10<sup>-4</sup> m<sup>3</sup>/s, respectively. Table 1 lists the input parameters used for the HM-PNM simulations.

## 2.3 Simulation Results

Upon injection of immiscible fluids into water-saturated deformable porous media, a variety of the flow patterns and deformation features are observed while varying their interfacial tension and viscosity, as shown in Fig. 2. Note that the black dots represent the node positions for particles and the circle among the black dots represents the pore among particles. The color of the pore indicates the saturation of an invading fluid; the pores filled with water (defending fluid) are expressed as white, and those completely filled with the invading fluid are denoted in sky blue color. Inlet pores are shown in blue color. This section discusses the effects of various conditional factors used in the parametric study, which includes the viscosity of the invading fluid, fluid injection rate, interfacial tension, effective grain modulus, and effective boundary stress.

### 2.3.1 Viscosity of the Invading Fluid $\mu_{in}$

The viscosity ratio of invading and defending fluids, referred to as the mobility ratio ( $M$ ), has a profound effect on fluid invasion patterns (Aker et al. 1998; Chang et al. 2019; Culligan et al. 2006; Kueper et al. 1989; Lenormand et al. 1988; Zhang et al. 2011; Zheng et al. 2017). The HM-PNM simulation results shown in Fig. 2a confirm the viscous

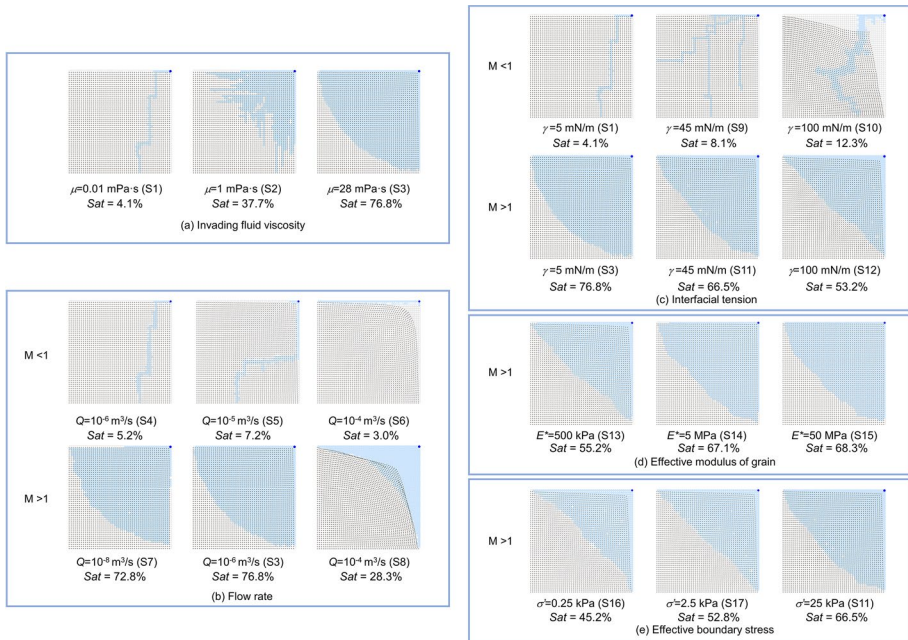


**Fig. 2** HM-PNM simulation results: **a** effect of invading fluid viscosity, **b** effect of flow rate, **c** effect of interfacial tension, **d** effect of effective modulus of grain, and **e** effect of effective confining stress. Note: the black dots represent nodes and sky blue circles show pores with an invading fluid, while hollow circles represent pores with a defending fluid. *Sat* indicates the saturation of the invading fluid

fingering pattern when a low viscosity fluid is injected ( $M < 1$ ) and the stable displacement occurring with the injection of a high viscous fluid ( $M > 1$ ). As a result, an increase in the viscosity of the invading fluid leads to an increase in the invading fluid saturation at percolation and hence an increase in the sweep efficiency. Furthermore, as the viscosity increases, the injection pressure increases at a given injection rate, which in turn causes mechanical deformation of the medium (e.g., Case S3 with  $\mu_{in} = 28 \text{ mPa}\cdot\text{s}$ ). Therefore, it is expected that the deformation becomes more significant as the invading fluid viscosity increases, attributable to the increased injection pressure and the elevated viscous drag force. This is consistent with the experiment results reported in Zadeh et al. (2023) and with the simulation results reported in Jeon et al. (2020a, b).

### 2.3.2 Flow Rate $Q$

The fluid pressure at the injection well, herein the injection pore, is directly proportional to the fluid injection rate (or flow rate  $Q$ ). Accordingly, the higher flow rate causes the more severe deformation in association with the increased injection pressure, as illustrated in Fig. 2b. This is consistently observed in both high and low mobility conditions (e.g.,  $M > 1$  and  $M < 1$ ). Meanwhile, when the mobility ratio is high, the greater deformation is observed due to the increased viscous drag force. Furthermore, it is worth noting that the saturation of the invading fluid at percolation decreases as the flow rate increases when the fluid flows in a stable displacement manner with  $M > 1$ , from  $Sat \approx 70\%$  with

$Q=10^{-8}$  m<sup>3</sup>/s to Sat $\approx$ 30% with  $Q=10^{-4}$  m<sup>3</sup>/s. This is because the induced pressure gradient displaces grain nodes toward boundaries, increasing throat radius at the center. It leads to the preferential flow in the pore network, resulting in the faster percolation for a given flow rate. These observations are in agreement with the experimental results reported by Zadeh et al. (2023).

### 2.3.3 Interfacial Tension $\gamma$

The interfacial tension between two immiscible fluids  $\gamma$  as well as the wettability of the invading fluid to the host porous medium determines the capillary pressure at the interface of two immiscible fluids. The pressure of the invading fluid must exceed the capillary pressure to invade; therefore, the capillary pressure acts as a barrier against fluid invasion. The parametric study varied the interfacial tension to examine the effect of capillary pressure (or capillarity) while the wettability was kept unchanged. The simulation results shown in Fig. 2c indicate that the greater deformation occurs as the interfacial tension increases. This is primarily attributed to the increased injection pressure with the increased capillary pressure. Again, when the stable displacement occurs with  $M > 1$ , the saturation of the invading fluid decreases as the extent of deformation becomes more significant (Fig. 2c). By contrast, when a low viscosity  $M < 1$  with a high interfacial tension (e.g., Case S10), a preferential flow path with significant deformation is developed due to the capillary and viscous fingering. Such a preferential flow occurrence in the cases with low viscosity ( $M < 1$ ) is because the pressure difference overcomes capillary pressure at only a few selected throats in the heterogenous network. The increase of injection pressure by high interfacial tension (e.g., with  $\gamma = 100$  mN/m) leads to significant deformation and reduces a variation in pore size, resulting in a wider flow channel. This suggests that deformation modifies the pore structures by opening or closing pore throats, and affects the preferential flow pattern.

### 2.3.4 Effective Modulus of Grain $E^*$

The effective modulus of grain  $E^*$  determines the contact stiffness and thus the spring stiffness in HM-PNM. Accordingly, as the effective modulus increases, the medium stiffness increases. It appears that the immiscible fluid injection causes less deformation as the medium stiffness increases, as demonstrated in Fig. 2d. While deformation manifests with  $E^* = 500$  kPa, no or only minimal deformation occurs with  $E^* = 50$  MPa.

### 2.3.5 Effective Confining Stress $\sigma'$

In a similar manner with the effective grain stiffness, the effective confining stress also increases the contact stiffness between grains and hence the spring stiffness in HM-PNM according to Hertzian contact theory. Therefore, an increase in the effective confining stress shows the same effect of the increased medium stiffness. The HM-PNM developed in this study incorporates the effective confining stress by controlling the initial spring contraction which in turn affects the initial spring stiffness. The simulation results shown in Fig. 2e demonstrate that an increase in the effective confining stress reduces the flow-induced deformation. Expectedly, a low effective confining stress allows deformation, which reduces the invading fluid saturation at percolation (e.g., Sat=45.2% with  $\sigma' = 0.25$  kPa



at Case S16 vs.  $Sat=66.5\%$  with  $\sigma' = 25$  kPa at Case S11). This result corroborates the Hele–Shaw experiment presented in Zadeh et al. (2023) and has the same trend with gas migration experiment results using transparent soil in Sun and Santamarina (2019).

### 3 Analysis and Discussion: Dimensionless Analyses

The parametric study using HM-PNM reveals that all the parameters act in combination; therefore, a single parameter is not sufficient to capture the flow-driven deformation during two-phase immiscible fluid flows. The simulation results are classified into four categories according to the flow pattern (stable displacement versus fingering invasion) and deformation occurrence (deformation versus no deformation). The extent of deformation is assessed with the maximum particle displacement until percolation. Displacement of each particle can be determined with the root mean-squared displacement (RMSD), defined as the addition of x-direction displacement and y-direction displacement, *i.e.*,  $RMSD = (\delta_x^2 + \delta_y^2)^{0.5}$ . The maximum value of RMSD at a given time among all the particles selected to capture the displacement of a certain particle that undergoes the most substantial movement during fluid injection. Accordingly, the maximum RMSD indicates the maximum local displacement possible during HM-PNM simulations. This study sets the criterion of RMSD for deformation occurrence as 10% of the particle diameter, which is 0.2 mm. This section examines the classified HM-PNM results with various dimensionless parameters that are relevant to the hydromechanical processes. Herein, to cover wide ranges of parameters, additional HM-PNM simulations were carried out, as listed in Table 2. In addition, the Hele–Shaw experiment results from the previous literature (Jeon et al. 2020a; Zadeh et al. 2023) are also compiled and compared with the HM-PNM simulation results, which cross-validates the simulation results, as summarized in Table 3. Section 3.1 aims to examine whether the flow pattern is affected by the deformation and the flow regime boundaries in the two-phase diagram ( $Ca$ – $M$  diagram) are effective in soft deformable porous media. The following sections are dedicated to assess capability of previously proposed dimensionless parameters in the literature and newly proposed ones in this study in predicting the occurrence of flow-driven deformation in deformable porous media.

#### 3.1 Two-Phase Flow Diagram with Capillary Number ( $Ca$ ) and Mobility Ratio ( $M$ )

A two-phase flow diagram using capillary number ( $Ca$ ) and mobility ratio ( $M$ ), or  $Ca$ – $M$  diagram, is widely used and validated in non-deformable porous media (Chang et al. 2019; DeHoff et al. 2012; Ferer et al. 2004; Lenormand et al. 1988; Wang et al. 2013; Zhang et al. 2011; Zheng et al. 2017). The capillary number ( $Ca$ ) is the ratio of viscous force to capillary force and the mobility ratio ( $M$ ) indicates the ratio of viscosities of invading and defending fluids. When both  $M$  and  $Ca$  are sufficiently high, an immiscible fluid shows a stable displacement pattern, whereas an immiscible fluid invades with a fingering pattern when  $M$  is small, *i.e.*, viscous fingering, or when  $Ca$  is small, *e.g.*, capillary fingering. Figure 3 plots and compares the flow pattern results from the HM-PNM simulations in the two-phase flow  $Ca$ – $M$  diagram. Regardless of deformation occurrence, the immiscible flow simulation results well capture the viscous fingering and stable displacement, which appears to be consistent with the boundaries suggested

**Table 2** Input parameters and dimensionless numbers for additional HM-PNM simulation cases

Case #	$\gamma$ (mN/m)	$\mu_{in}$ (mPa·s)	$Q$ (m <sup>3</sup> /s)	$E^*$ (kPa)	$\sigma'$ (kPa)	$F_s/F_{sk}$	$F_c/F_{sk}$	$P_c/P_{frac}$	$P_v/P_{frac}$
S18	45	28	10 <sup>-6</sup>	1,000,000	250	1.68 × 10 <sup>-4</sup>	1.41 × 10 <sup>-4</sup>	3.89 × 10 <sup>-4</sup>	1.16 × 10 <sup>-4</sup>
S19	45	28	10 <sup>-6</sup>	500,000	25	1.68 × 10 <sup>-3</sup>	1.41 × 10 <sup>-3</sup>	1.03 × 10 <sup>-3</sup>	3.06 × 10 <sup>-4</sup>
S20	45	28	10 <sup>-6</sup>	5000	25	1.68 × 10 <sup>-3</sup>	1.41 × 10 <sup>-3</sup>	4.50 × 10 <sup>-3</sup>	1.34 × 10 <sup>-3</sup>
S21	45	28	10 <sup>-6</sup>	50,000	25	1.68 × 10 <sup>-3</sup>	1.41 × 10 <sup>-3</sup>	2.49 × 10 <sup>-3</sup>	7.38 × 10 <sup>-4</sup>
S22	5	28	10 <sup>-7</sup>	500	25	1.68 × 10 <sup>-4</sup>	1.57 × 10 <sup>-4</sup>	7.52 × 10 <sup>-4</sup>	2.01 × 10 <sup>-4</sup>
S23	45	0.01	10 <sup>-6</sup>	500	2.5	6.00 × 10 <sup>-6</sup>	1.41 × 10 <sup>-2</sup>	2.49 × 10 <sup>-2</sup>	2.64 × 10 <sup>-6</sup>
S24	45	1	10 <sup>-8</sup>	500	25	6.00 × 10 <sup>-7</sup>	1.41 × 10 <sup>-3</sup>	6.05 × 10 <sup>-3</sup>	6.42 × 10 <sup>-7</sup>
S25	5	0.1	10 <sup>-6</sup>	500	25	6.00 × 10 <sup>-6</sup>	1.57 × 10 <sup>-4</sup>	7.52 × 10 <sup>-4</sup>	7.19 × 10 <sup>-6</sup>
S26	100	1	10 <sup>-6</sup>	500	2.5	6.00 × 10 <sup>-4</sup>	3.14 × 10 <sup>-2</sup>	4.18 × 10 <sup>-2</sup>	2.00 × 10 <sup>-4</sup>
S27	45	0.01	10 <sup>-6</sup>	1,000,000	25	6.00 × 10 <sup>-7</sup>	1.41 × 10 <sup>-3</sup>	7.59 × 10 <sup>-4</sup>	8.05 × 10 <sup>-8</sup>
S28	45	0.01	10 <sup>-4</sup>	1,000,000	25	6.00 × 10 <sup>-5</sup>	1.41 × 10 <sup>-3</sup>	7.59 × 10 <sup>-4</sup>	8.05 × 10 <sup>-6</sup>
S29	45	0.01	10 <sup>-2</sup>	1,000,000	25	6.00 × 10 <sup>-3</sup>	1.41 × 10 <sup>-3</sup>	7.59 × 10 <sup>-4</sup>	8.05 × 10 <sup>-4</sup>
S30	45	28	10 <sup>-10</sup>	500	0.25	1.68 × 10 <sup>-5</sup>	1.41 × 10 <sup>-1</sup>	3.60 × 10 <sup>-2</sup>	1.07 × 10 <sup>-6</sup>
S31	5	28	10 <sup>-10</sup>	500	0.25	1.68 × 10 <sup>-5</sup>	1.57 × 10 <sup>-2</sup>	1.09 × 10 <sup>-2</sup>	2.92 × 10 <sup>-6</sup>
S32	5	28	10 <sup>-10</sup>	50,000	0.25	1.68 × 10 <sup>-5</sup>	1.57 × 10 <sup>-2</sup>	1.25 × 10 <sup>-3</sup>	3.33 × 10 <sup>-7</sup>
S33	5	28	10 <sup>-10</sup>	1000	0.25	1.68 × 10 <sup>-5</sup>	1.57 × 10 <sup>-2</sup>	8.04 × 10 <sup>-3</sup>	2.15 × 10 <sup>-6</sup>
S34	5	28	10 <sup>-12</sup>	1000	0.25	1.68 × 10 <sup>-7</sup>	1.57 × 10 <sup>-2</sup>	8.04 × 10 <sup>-3</sup>	2.15 × 10 <sup>-8</sup>
S35	5	0.01	10 <sup>-8</sup>	1000	2.5	6.00 × 10 <sup>-8</sup>	1.57 × 10 <sup>-3</sup>	4.22 × 10 <sup>-3</sup>	4.03 × 10 <sup>-8</sup>
S36	45	28	10 <sup>-6</sup>	500	250	1.68 × 10 <sup>-4</sup>	1.41 × 10 <sup>-4</sup>	7.07 × 10 <sup>-4</sup>	2.10 × 10 <sup>-4</sup>
S37	45	28	10 <sup>-6</sup>	5000	2.5	1.68 × 10 <sup>-2</sup>	1.41 × 10 <sup>-2</sup>	1.03 × 10 <sup>-2</sup>	3.06 × 10 <sup>-3</sup>
S38	5	28	10 <sup>-11</sup>	1000	2.5	1.68 × 10 <sup>-7</sup>	1.57 × 10 <sup>-3</sup>	4.22 × 10 <sup>-3</sup>	1.13 × 10 <sup>-7</sup>
S39	5	0.01	10 <sup>-11</sup>	1000	2.5	6.00 × 10 <sup>-11</sup>	1.57 × 10 <sup>-3</sup>	4.22 × 10 <sup>-3</sup>	4.03 × 10 <sup>-11</sup>
S40	5	0.01	10 <sup>-4</sup>	1000	25	6.00 × 10 <sup>-5</sup>	1.57 × 10 <sup>-4</sup>	7.34 × 10 <sup>-4</sup>	7.01 × 10 <sup>-5</sup>
S41	5	0.1	10 <sup>-8</sup>	1000	25	6.00 × 10 <sup>-8</sup>	1.57 × 10 <sup>-4</sup>	7.34 × 10 <sup>-4</sup>	7.01 × 10 <sup>-8</sup>
S42	5	28	10 <sup>-12</sup>	50,000	3.75	1.12 × 10 <sup>-8</sup>	1.05 × 10 <sup>-3</sup>	1.02 × 10 <sup>-3</sup>	2.73 × 10 <sup>-9</sup>
S43	45	0.01	10 <sup>-10</sup>	50,000	2.5	6.00 × 10 <sup>-10</sup>	1.41 × 10 <sup>-2</sup>	3.60 × 10 <sup>-3</sup>	3.82 × 10 <sup>-11</sup>
S44	45	28	10 <sup>-10</sup>	50,000	3.75	1.12 × 10 <sup>-6</sup>	9.42 × 10 <sup>-3</sup>	3.52 × 10 <sup>-3</sup>	1.04 × 10 <sup>-7</sup>
S45	45	28	10 <sup>-9</sup>	500	25	1.68 × 10 <sup>-6</sup>	1.41 × 10 <sup>-3</sup>	6.05 × 10 <sup>-3</sup>	1.80 × 10 <sup>-6</sup>
S46	45	28	10 <sup>-11</sup>	500	25	1.68 × 10 <sup>-8</sup>	1.41 × 10 <sup>-3</sup>	6.05 × 10 <sup>-3</sup>	1.80 × 10 <sup>-8</sup>
S47	0.5	0.01	10 <sup>-6</sup>	500	25	6.00 × 10 <sup>-7</sup>	1.57 × 10 <sup>-5</sup>	7.84 × 10 <sup>-5</sup>	7.49 × 10 <sup>-7</sup>
S48	45	28	10 <sup>-6</sup>	1,000,000	0.25	1.68 × 10 <sup>-1</sup>	1.41 × 10 <sup>-1</sup>	8.48 × 10 <sup>-4</sup>	2.52 × 10 <sup>-4</sup>
S49	45	28	10 <sup>-10</sup>	1,000,000	250	1.68 × 10 <sup>-8</sup>	1.41 × 10 <sup>-4</sup>	3.89 × 10 <sup>-4</sup>	1.16 × 10 <sup>-8</sup>
S50	450	28	10 <sup>-6</sup>	1,000,000	250	1.68 × 10 <sup>-4</sup>	1.41 × 10 <sup>-3</sup>	1.95 × 10 <sup>-3</sup>	5.81 × 10 <sup>-5</sup>

in previous literature (Lenormand et al. 1988; Zhang et al. 2011). Note that this study classified the patterns into two classes, stable displacement or fingering. Therefore, the results near the mobility ratio of  $\log M=0$  are classified as fingering due to their low fluid saturations, although they are placed in the transition zone between the stable displacement and fingering (Fig. 3).

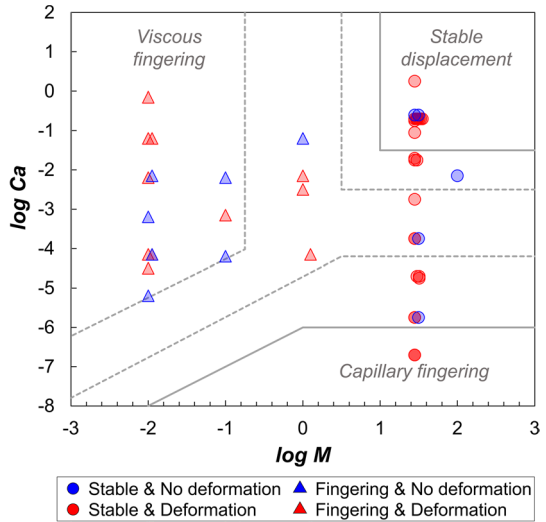
**Table 3** Test conditions of experimental study

Case #	Porous media	Invading fluid	Defending fluid	Flow rate (ml/min)	Particle size <sup>a</sup> (mm)	$F_s/F_{sk}$	$F_c/F_{sk}$	$P_c/P_{frac}$	$P_s/P_{frac}$
E1	Hydrogel ( $E = 50$ kPa)	Mineral oil ( $\mu_{in} = 28$ mPa·s)	Water ( $\mu_{def} = 1$ mPa·s)	10	1.24	5.61	8.16	$1.15 \times 10^{-1}$	$3.96 \times 10^{-2}$
E2					1.62	0.22	0.32	$9.03 \times 10^{-2}$	$3.10 \times 10^{-2}$
E3					1.90	0.16	0.23	$8.08 \times 10^{-2}$	$2.78 \times 10^{-2}$
E4					1.24	56.07	8.16	$1.15 \times 10^{-1}$	$3.96 \times 10^{-1}$
E5	Glass bead ( $E = 3.1$ GPa)			100	1.62	2.21	0.32	$9.03 \times 10^{-2}$	$3.10 \times 10^{-1}$
E6					1.90	1.60	0.23	$8.08 \times 10^{-2}$	$2.78 \times 10^{-1}$
E7					1.59	3.39	4.94	$4.11 \times 10^{-4}$	$1.41 \times 10^{-4}$
E8						33.94	4.94	$4.11 \times 10^{-4}$	$1.41 \times 10^{-4}$

All the test data were extracted from Zadeh et al. (2023)

<sup>a</sup>The hydrogel was fully saturated for 24 h, and the dimensionless parameters were calculated by using the average hydrogel particle diameter

**Fig. 3** A two-phase diagram of capillary number ( $Ca$ ) and mobility ratio ( $M$ ). Gray solid lines show the flow regime boundary from Lenormand et al. (1988), and gray dotted lines are adapted from Zhang et al. (2011)



### 3.2 Dimensionless Analysis with Particle-Level Forces

Recent studies have suggested the particle-level forces to explain the mechanical deformation ensued with two-phase flows in porous media (Han et al. 2020; Jeon et al. 2020a; Shin and Santamarina 2010; Zadeh et al. 2023). The particle-level forces associated with fluid flows in porous media include the viscous seepage force  $F_v$ , the capillary force  $F_c$ , and the skeletal force  $F_{sk}$ ; their ratios are adopted as indicators to occurrence of flow-driven deformation (Jeon et al. 2020a; Shin and Santamarina 2010). The dimensionless map of particle-level force ratios proposed by Shin and Santamarina (2010) suggests the seepage force ratio ( $F_v/F_{sk}$ ) and the capillary force ratio ( $F_c/F_{sk}$ ) to classify the hydraulic fracture into three regimes: capillary-driven opening, drag-driven opening, or mixed-mode opening. The viscous seepage force can be estimated using Stokes' drag force, *i.e.*,  $F_v = 6\pi\mu aV$ , where  $V$  is flow velocity,  $\mu$  is fluid viscosity, and  $a$  is the grain radius. The capillary force exerted on the interfaces between two immiscible fluids is defined by Young–Laplace equation, *i.e.*,  $F_c = \pi a \gamma$ , where  $\gamma$  is the interfacial tension. Lastly, the skeletal force is defined as  $F_{sk} = 4a^2 \sigma'$ , where  $\sigma'$  is the effective stress which the grain should carry on. In the HM-PNM, the skeletal force is assumed to be the Hertzian contact force required to pull apart the compressed two grains with an initial spring contraction  $h_o$ , *i.e.*,  $F_{sk} = (4/3) \cdot E^* \cdot (a/2)^{1/2} \cdot h_o^{3/2}$ .

The relevant forces are calculated for each case, and the classified HM-PNM results are plotted on the dimensionless map using the corresponding seepage force ratio and capillary force ratio, as shown in Fig. 4. As expected, the simulation results show a consistent tendency with Shin and Santamarina (2010), where deformation occurs with increases in the seepage force ratio and capillary force ratio. However, some cases are placed out of tendency, which includes Cases S48, S17, S35, and S46 (Fig. 4b). When comparing Cases S48 and S17, although Case S48 has the higher capillary force ratio ( $F_c/F_{sk}$ ) and the higher seepage force ratio ( $F_v/F_{sk}$ ) than Case S17, not Case S48 but Case S17 shows deformation. Similarly, Case S46 shows deformation occurrence despite of its low seepage force ratio compared to that of Case S35 (Fig. 4b). These differences are mainly attributable to the grain stiffness, which is related to the medium stiffness (*i.e.*,  $E = K/(2 \cdot a) = E^* \sqrt{h/(2 \cdot a)}$ ).

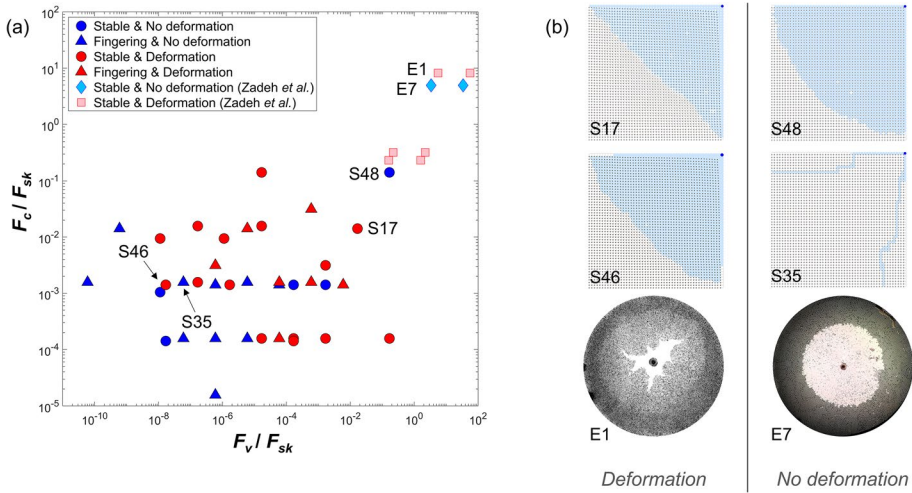


**Fig. 4** **a** Dimensionless map with the particle-level force ratios and **b** representative results of HM-PNM and Hele–Shaw experiments to compare. Cases E1 and E7: Mineral oil (white) is injected into a granular medium saturated with water (dark gray; Zadeh et al. 2023). Cases S17, S35, S46, and S48: the color of pores represents the saturation of invading fluid (sky blue: 100%, white: 0%) and black small dots show the particle positions

Hence, the particle-level force ratios appear not able to capture the effect of grain modulus, particularly when the grain modulus is low.

Previously reported Hele–Shaw cell experiment data from Zadeh et al. (2023) are also superimposed in Fig. 4. These experimental results from mineral oil injection into water-saturated media are categorized into two groups with and without deformation, in all of which fluid invaded in a stable manner. The test images after 50 s injection in Cases E1 and E7 are shown in Fig. 4b, where mineral oil was injected into a water-saturated glass bead medium and a water-saturated hydrogel medium, respectively. In the hydrogel medium (Case E1), fracture-like deformation was observed in the host porous media. By contrast, no mechanical change was observed in the glass bead medium due to its high grain stiffness (Case E7). Apparently, although Cases E1 and E7 showed distinctly different deformation patterns, their capillary force ratio ( $F_c / F_{sk}$ ) and seepage force ratio ( $F_v / F_{sk}$ ) are similar and thus placed close each other in the dimensionless map of particle-level force ratios (Fig. 4a). The effective stress used in the  $F_{sk}$  computation is determined based on the overburden weight of the cover glass plate or the self-weight of the silica gels and glass beads in the experiments (Zadeh et al. 2023), and the grain stiffness has no influence on the skeletal force. Therefore, the particle-level skeletal force, as defined by Shin and Santamarina (2010), appears insufficient to predict the deformation occurrence in soft deformable porous media.

### 3.3 Dimensionless Analyses with Various Parameters

The HM-PNM simulation results are also analyzed with the hydromechanical parameters proposed by Huang et al. (2012) and Holtzman and Juanes (2010). Huang et al. (2012) adopted dimensionless characteristic times  $\tau_1$  and  $\tau_2$ , and they identified four regimes for viscous fluid

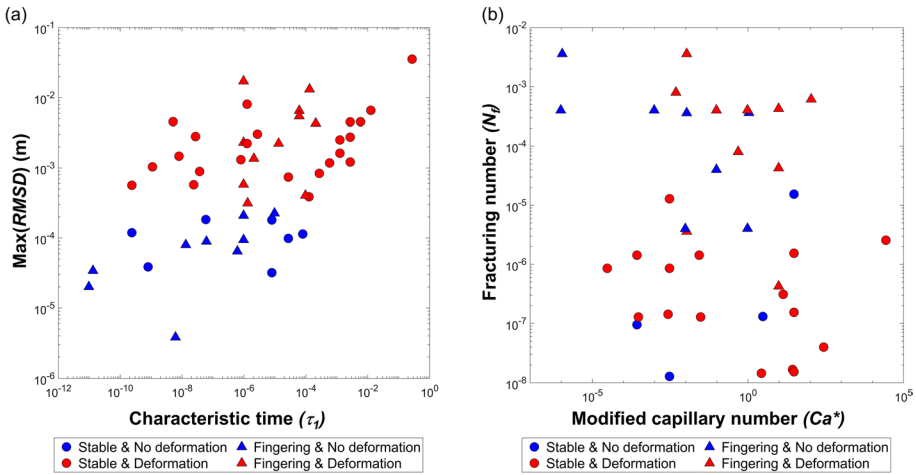


**Fig. 5** Simulation results using previously proposed parameters: **a** the characteristic time ( $\tau_1$ ) by Huang et al. (2012) and **b** the modified capillary number ( $Ca^*$ ) and fracturing number ( $N_f$ ) by Holtzman and Juanes (2010)

injection into dry granular media, which are the simple-radial flow regime, filtration-dominant regime, grain displacement-dominant regime, and viscous fingering-dominant regime, respectively. The dimensionless characteristic time  $\tau_1$  is the ratio of the diffusion time scale ( $t_d = \mu^2/E/k$ ) to the injection time scale ( $t_i = l/V$ ), where  $k$  is the intrinsic permeability, and  $l$  is the characteristic length ( $l = 2 \cdot a$ ) (Huang et al. 2012). The dimensionless characteristic time  $\tau_2$  is the ratio of the retardation time scale ( $t_r = \mu'/E$ ) to the injection time scale ( $t_i$ ), where  $\mu'$  is the apparent viscosity of the granular medium, which is one class of the effective viscosity for particle-mixed fluids, e.g., suspension (Huang et al. 2012).

The simulation cases used in this study only exhibit the simple-radial flow regime and filtration-domination regime, and these regimes are determined solely by  $\tau_1$ . Accordingly, the dimensionless characteristic time ( $\tau_1$ ) of the HM-PNM simulation results is compared to their maximum RMSD as an indicator to the extent of deformation, as shown in Fig. 5a. In this study, it is assumed that the apparent viscosity of grain medium  $\mu'$  is identical to the viscosity of injecting fluid as the grains hardly flow with fluids in this study (i.e.,  $\mu' = \mu \cdot f(\phi)$  and  $f(\phi) = 1$ ). The result shows that in general the deformation becomes greater as the dimensionless characteristic time ( $\tau_1$ ) increases. However, it appears that the RMSD significantly varies even at the same dimensionless characteristic time ( $\tau_1$ ), which suggests that the characteristic time alone is insufficient to be used as an indicator to the extent of deformation. This may be due to the lack of capillary effect in calculating the characteristic time ( $\tau_1$ ). The previous study by Huang et al. (2012) used air and glycerol, which are miscible each other; the capillary effect was negligible. However, in the present study, the capillary force plays a significant role in the hydromechanical process at the interface of two immiscible fluids.

The fracturing number ( $N_f$ ) and the modified capillary number ( $Ca^*$ ) have been suggested to explain the transition from fingering to fracture in granular media (Holtzman et al. 2012; Holtzman and Juanes 2010). The fracturing number ( $N_f$ ) is defined as the ratio of the driving pressure force to the resisting force, which is the interparticle forces holding the particles (i.e.,  $N_f = \frac{\sqrt{2}\gamma}{\lambda E^*(ah)^2}$ ). The modified capillary number

number ( $Ca^*$ ) is defined as the dimensionless number at which the flow regime changes from viscous fingering to capillary fingering, *i.e.*,  $Ca^* = Ca \frac{L}{2a} \chi^{-1}(\lambda)$ , where  $\lambda$  is the disorder coefficient with  $\chi(\lambda) = \lambda/(1 - \lambda^2)$ ,  $L$  is macroscopic length scale,  $L = 2 \cdot a \cdot n$ , and  $n$  is the number of grain in the network, in this study  $n = 50$ . The map using the fracturing number and the modified capillary number ( $Ca^*$ ) has shown to accurately capture the transition boundaries from fingering to fracturing when air is injected into water-saturated stiff granular media.

The suitability of the modified capillary number and fracturing number is evaluated for the simulation cases in this study by using the suggested equations, as shown in Fig. 5b. Holtzman and Juanes (2010) estimated the fracturing number by assuming the frictional force as the dominant resisting force. However, in a soft granular particle such as hydrogel, the elastic behavior is dominant over the frictional behavior. Therefore, there was no consistent boundary delineating the deformation with the fracturing number.

### 3.4 Dimensionless Analysis with Particle-Level Pressure Ratios

The aforementioned dimensionless parameters such as particle-level force ratio, characteristic time, and fracturing number show their limitations, especially in soft deformable porous media. This study explores the use of the dimensionless ratios based on the fracture pressure for predicting the deformation occurrence caused by immiscible flow injection in porous media. The fracture pressure has been introduced to explain gas migration patterns in granular media and elucidate the effect of particle size or confining stress (Jain and Juanes 2009; Lee et al. 2020). According to the linear-elastic fracture mechanics, the fracture pressure can be calculated as  $P_{\text{frac}} = \sqrt{\gamma E/l + |\sigma_o t|}$ , where  $E$  is the representative elastic modulus of packing (medium stiffness  $E$  is used here),  $\gamma$  is the interfacial tension, and  $l$  is the crack tip length (Johnson 1987). The crack tip length is assumed to be equivalent to the particle diameter in this study, *i.e.*,  $l = 2a$ . Zadeh et al. (2023) have firstly introduced the ratios of the capillary pressure and the viscous drag pressure to the fracture pressure for the dimensionless analysis. These dimensionless pressure ratios are referred to as the capillary pressure ratio,  $P_c/P_{\text{frac}}$  and the viscous pressure ratio,  $P_v/P_{\text{frac}}$ , where the capillary pressure  $P_c$  is  $2\gamma/r$  (where  $r = a/2$ ) and the viscous drag pressure  $P_v$  is  $6\mu V/a$ , respectively.

Figure 6a shows the map based on the capillary pressure ratio and viscous pressure ratio with HM-PNM simulation results as well as the Hele–Shaw experiment results (Tables 2 and 3). The map depicts that fluid-driven deformation is more likely to occur as the viscous pressure ratio and the capillary pressure ratio increase. The dimensionless pressure ratio-based map provides a clear trend in predicting deformation occurrence, compared to the map based on the particle-level forces. Moreover, Cases E7, E1, S48, and S17 that were indistinguishable with the particle-level force ratios can be readily categorized into different regimes in the pressure ratio map, though Cases S35 and S46 are still hard to distinguish. Figure 6b highlights the extent of deformation in each HM-PNM simulation case with color according to the maximum RMSD. More severe deformation occurs as the capillary pressure ratio or the viscous pressure ratio increases.

The map can be divided into four regimes: no deformation regime, capillary-induced deformation regime, drag-driven deformation regime, and mixed-mode deformation regime. The capillary-induced deformations are expected when the capillary pressure ratio  $P_c/P_{\text{frac}}$  is greater than  $\sim 10^{-1}$ , and there is a transient zone from no deformation to capillary-induced deformation for  $P_c/P_{\text{frac}} = 10^{-3} - 10^{-1}$ . The drag-driven deformation

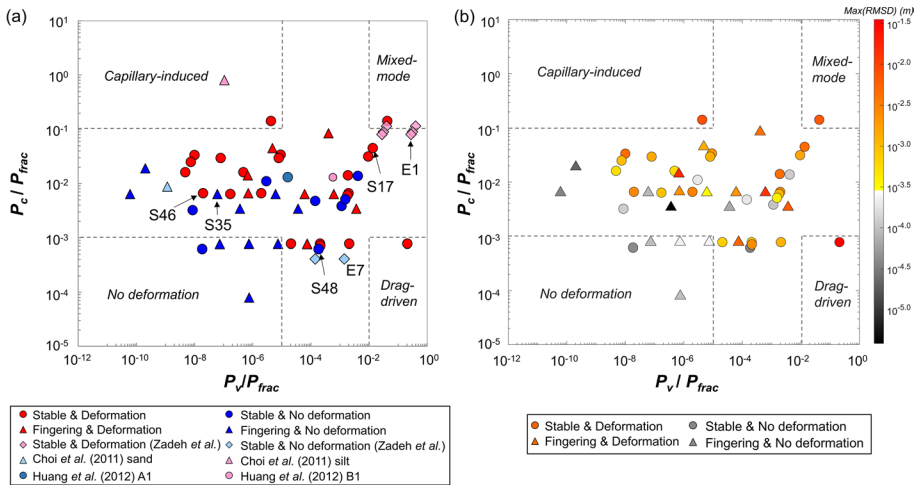


**Fig. 6** Dimensionless map using the particle-level pressure ratios: **a** deformation occurrence, and **b** maximum root mean-squared displacement (RMSD). Note that the results in Panel (a) are gathered from the HM-PNM simulations of this study and experimental results by Zadeh et al. (2023), Choi et al. (2011), and Huang et al. (2012), and those in Panel (b) are derived from the HM-PNM simulation of this study

boundary is expected at the viscous pressure ratio  $P_v/P_{frac} \approx 10^{-2}$ . These boundaries agree well with those reported in the previous experimental investigation by Zadeh et al. (2023). The results suggest that the dimensionless ratios based on the pressure ratios well delineate the regimes for flow-driven deformation, where the capillary force and the viscous drag force act as dominant driving forces.

Additionally, previously published results, derived Hele–Shaw experiments by Choi et al. (2011) and Huang et al. (2012), are superimposed in Fig. 6a to examine the validity of the proposed dimensionless map. Pink color indicates the cases with fracturing or conduit opening (the case with silt from Choi et al. 2011; Case A1 from Huang et al. 2012). Light blue or deep blue color indicates the cases with no deformation (the case with sand from Choi et al. 2011; Case B1 from Huang et al. 2012). Some parameters were reasonably assumed due to the limited information available in the literature. The injection velocity was computed based on the average velocity during injection (3 ml/min) and an assumed port inner diameter (1 mm). The medium stiffness was estimated using an empirical equation based on the effective confining stress, proposed by Cha et al. (2014), i.e.,  $E = 2 \cdot (1 + \nu) \cdot \rho \cdot V_S^2$ , where  $V_S$  is  $\alpha \cdot (\sigma' / 1 \text{ kPa})^\beta$ ,  $\nu = 0.25$ ,  $\rho = 2.5$ ,  $\alpha = 50$ , and  $\beta = 0.3$ . The pressure ratios for the silt case in Choi et al. (2011) belong to the capillary-induced deformation regime, but those for the sand case fall within the transition regime. Both the results of A1 and B1 from Huang et al. (2012) are placed in the transitions regime though grain displacement occurred in Case B1 due to the higher viscous pressure ratio than Case A1. In general, the Hele–Shaw experiment results conducted in previous studies appear to be well consistent with the pressure ratio boundaries delineated in our study.

Furthermore, the results reveal a power relationship between the maximum RMSD and the ratio of maximum injection pressure to medium stiffness ( $P_{max}/E$ ), as shown in Fig. 7a. The representative examples (Cases S8 to S49) demonstrate that the degree of opening increases with  $P_{max}/E$  (Fig. 7b). This implies that the injection pressure, together with the medium stiffness, plays a primary role in determining the deformation. It is because the



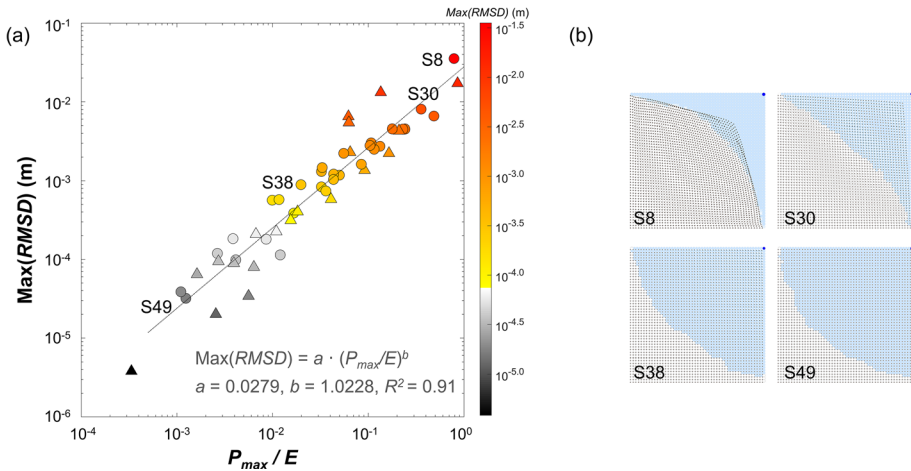


**Fig. 7** **a** The maximum RMSD versus the ratio of maximum injection pressure to equivalent medium stiffness, and **b** patterns of fluid flow and mechanical deformation in the representative cases. The regression line shows the relation between the maximum RMSD and  $P_{max}/E$

injection pressure determines the pore pressure in the vicinity of the inlet pores, which gradually attenuates to the outlet pores. During a fluid flow, the pore pressure decreases from the inlet pores to the outlet pores, creating the pore-to-pore pressure gradients. Such pore-to-pore pressure gradients determine the spring contraction and grain deformation in the HM-PNM. On the other hand, the medium stiffness reflects the resistance to external forces, particularly the pore pressure in this study. In this regard,  $P_{max}/E$  shows a good correlation with the extent of deformation.

In theory, the transition from one regime to another in the pressure-based dimensionless map is assumed to happen near the value of 1. From Jeon et al. (2020a) and Zadeh et al. (2023) and through this study, however, the transitional regions seem to occur at values lower by one to three orders of magnitudes. Numerically, this might be related to several simplifications and assumptions incorporated in this study to streamline our model. For instance, our model only accounts for the normal force based on the Hertzian contact model, disregarding the shear force, and restricted the coordination number to four. Although previously reported experiment results by other research groups, as well as Zadeh et al. (2023), also corroborate our observations, there could be an effect of the boundary conditions. Therefore, it still necessitates further corroboration, and a more extensive research effort is essential to provide a deeper understanding of the flow-driven deformation in deformable porous or granular media.

## 4 Conclusion and Implications

Dimensionless analysis is a fundamental and efficient method for tackling complex hydro-mechanical problems, as it provides a systematic approach to reduce complexity, identify dominant factors, and gain insights into how systems behave under various conditions. In this study, a comprehensive dimensionless analysis is conducted on flow-driven deformation of granular porous media under immiscible fluid injection. The parametric analysis was

firstly performed using HM-PNM on invading fluid viscosity, flow rate, interfacial tension, grain modulus, and boundary stress. Our results reveal clear relationships: as the fluid viscosity, flow rate, and/or interfacial tension increases, the required injection pressure for a given flow rate also rises, leading to more pronounced mechanical deformation. Conversely, the higher grain modulus and boundary stress inhibit such mechanical changes.

Thereafter, the extensive simulation results are subjected to further dimensionless analyses. In conventional two-phase flow map using the capillary number and mobility ratio, the mechanical deformation effect is insignificant in determining the flow pattern and regime; however, it can affect the flow path development, changing in the saturation of invading fluid at percolation. Previously proposed dimensionless parameters such as particle-level force ratio, characteristic time, and fracturing number show some limited applicability for predicting deformation occurrence, especially in a soft porous media, whereas the particle-level pressure ratios based on capillary pressure and viscous drag pressure with respect to fracture pressure effectively capture the fluid-driven deformation even in a soft medium. A dimensionless map utilizing the capillary pressure ratio and viscous drag pressure ratio delineates four deformation regimes: no deformation, capillary-induced, drag-driven, and mixed-mode with the boundaries at  $10^{-1}$  of the capillary pressure ratio and at  $10^{-2}$  of the viscous drag pressure ratio. The increase in the capillary pressure ratio and viscous pressure ratio leads to the greater deformation. Moreover, the extent of deformation has a linear relationship with the ratio of the maximum fluid injection pressure to the medium stiffness.

This dimensionless analysis reveals that the capillary pressure ratio and viscous pressure ratio are effective in predicting the occurrence of deformation especially when injecting immiscible fluid, even in a soft porous medium. In many energy-related geo-engineering field, deformation or fracture by fluid injection is a critical issue. Our findings provide a useful tool for accessing flow-driven deformation under various injection conditions, applicable to many energy-geo-engineering fields.

**Acknowledgements** This work was supported under the framework of international cooperation program managed by National Research Foundation of Korea (2022K2A9A2A06044697) and by the Korea Institute of Energy Technology Evaluation and Planning (KETEP) grant, funded by the Korean Ministry of Trade, Industry & Energy (No. 20212010200020).

**Author Contributions** All authors contributed to the study conception and design. Data collection and analysis were performed by Min-Kyung Jeon. The first draft of the manuscript was written by Min-Kyung Jeon and all authors commented and edited on previous versions of the manuscript. All authors read and approved the final manuscript.

**Funding** Open Access funding enabled and organized by KAIST.

**Data Availability** The datasets generated during and/or analyzed during the current study are available from the corresponding author on reasonable request.

## Declarations

**Conflict of interest** The authors have no relevant financial or non-financial interest to disclose.

**Open Access** This article is licensed under a Creative Commons Attribution 4.0 International License, which permits use, sharing, adaptation, distribution and reproduction in any medium or format, as long as you give appropriate credit to the original author(s) and the source, provide a link to the Creative Commons licence, and indicate if changes were made. The images or other third party material in this article are included in the article's Creative Commons licence, unless indicated otherwise in a credit line to the material. If material is not included in the article's Creative Commons licence and your intended use is not permitted by statutory regulation or exceeds the permitted use, you will need to obtain permission directly from the copyright holder. To view a copy of this licence, visit <http://creativecommons.org/licenses/by/4.0/>.

## References

- Aker, E., Jørgen Måløy, K., Hansen, A., Batrouni, G.G.: A two-dimensional network simulator for two-phase flow in porous media. *Transp. Porous Media* **32**, 163–186 (1998). <https://doi.org/10.1023/A:1006510106194>
- Al-Gharbi, M.S., Blunt, M.J.: Dynamic network modeling of two-phase drainage in porous media. *Phys. Rev. E* **71**, 016308 (2005). <https://doi.org/10.1103/PhysRevE.71.016308>
- Atrazhev, V.V., Astakhova, T.Y., Dmitriev, D.V., Erikhman, N.S., Sultanov, V.I., Patterson, T., Burlatsky, S.F.: The model of stress distribution in polymer electrolyte membrane. *J. Electrochem. Soc.* **160**, F1129 (2013). <https://doi.org/10.1149/2.079310jes>
- Budday, S., Nay, R., de Rooij, R., Steinmann, P., Wyrobek, T., Ovaert, T.C., Kuhl, E.: Mechanical properties of gray and white matter brain tissue by indentation. *J. Mech. Behav. Biomed. Mater.* **46**, 318–330 (2015). <https://doi.org/10.1016/j.jmbbm.2015.02.024>
- Carrillo, F.J., Bourg, I.C.: Capillary and viscous fracturing during drainage in porous media. *Phys. Rev. E* **103**, 063106 (2021a). <https://doi.org/10.1103/PhysRevE.103.063106>
- Carrillo, F.J., Bourg, I.C.: Modeling multiphase flow within and around deformable porous materials: a Darcy-brinkman-biot approach. *Water Resour. Res.* **57**, e2020WR028734 (2021b). <https://doi.org/10.1029/2020WR028734>
- Carrillo, F.J., Bourg, I.C., Soulaine, C.: Multiphase flow modeling in multiscale porous media: an open-source micro-continuum approach. *J. Comput. Phys. X* **8**, 100073 (2020). <https://doi.org/10.1016/j.jcpx.2020.100073>
- Cha, M., Santamarina, J.C., Kim, H.-S., Cho, G.-C.: Small-strain stiffness, shear-wave velocity, and soil compressibility. *J. Geotech. Geoenviron. Eng.* **140**, 06014011 (2014). [https://doi.org/10.1061/\(ASCE\)GT.1943-5606.0001157](https://doi.org/10.1061/(ASCE)GT.1943-5606.0001157)
- Chang, C., Kneafsey, T.J., Zhou, Q., Oostrom, M., Ju, Y.: Scaling the impacts of pore-scale characteristics on unstable supercritical CO<sub>2</sub>-water drainage using a complete capillary number. *Int. J. Greenh. Gas Control* **86**, 11–21 (2019). <https://doi.org/10.1016/j.ijggc.2019.04.010>
- Cho, H.J., Lu, N.B., Howard, M.P., Adams, R.A., Datta, S.S.: Crack formation and self-closing in shrinkable, granular packings. *Soft Matter* **15**, 4689–4702 (2019). <https://doi.org/10.1039/C9SM00731H>
- Choi, J.-H., Seol, Y., Boswell, R., Juanes, R.: X-ray computed-tomography imaging of gas migration in water-saturated sediments: from capillary invasion to conduit opening. *Geophys. Res. Lett.* (2011). <https://doi.org/10.1029/2011GL048513>
- Culligan, K.A., Wildenschild, D., Christensen, B.S.B., Gray, W.G., Rivers, M.L.: Pore-scale characteristics of multiphase flow in porous media: a comparison of air–water and oil–water experiments. *Adv. Water Resour.* **29**, 227–238 (2006). <https://doi.org/10.1016/j.advwatres.2005.03.021>
- DeHoff, K.J., Oostrom, M., Zhang, C., Grate, J.W.: Evaluation of two-phase relative permeability and capillary pressure relations for unstable displacements in a pore network. *Vadose Zone J.* (2012). <https://doi.org/10.2136/vzj2012.0024>
- Ferer, M., Ji, C., Bromhal, G.S., Cook, J., Ahmadi, G., Smith, D.H.: Crossover from capillary fingering to viscous fingering for immiscible unstable flow: experiment and modeling. *Phys. Rev. E* **70**, 016303 (2004). <https://doi.org/10.1103/PhysRevE.70.016303>
- Franceschini, G., Bigoni, D., Regitnig, P., Holzapfel, G.A.: Brain tissue deforms similarly to filled elastomers and follows consolidation theory. *J. Mech. Phys. Solids* **54**, 2592–2620 (2006). <https://doi.org/10.1016/j.jmps.2006.05.004>
- Gutierrez, M., Katsuki, D., Tutuncu, A.: Determination of the continuous stress-dependent permeability, compressibility and poroelasticity of shale. *Mar. Pet. Geol.* **68**, 614–628 (2015). <https://doi.org/10.1016/j.marpetgeo.2014.12.002>
- Han, G., Kwon, T.-H., Lee, J.Y., Jung, J.: Fines migration and pore clogging induced by single- and two-phase fluid flows in porous media: from the perspectives of particle detachment and particle-level forces. *Geomech. Energy Environ.* **23**, 100131 (2020). <https://doi.org/10.1016/j.gete.2019.100131>
- Holtzman, R., Juanes, R.: Crossover from fingering to fracturing in deformable disordered media. *Phys. Rev. E* **82**, 046305 (2010). <https://doi.org/10.1103/PhysRevE.82.046305>
- Holtzman, R., Szulczewski, M.L., Juanes, R.: Capillary fracturing in granular media. *Phys. Rev. Lett.* **108**, 264504 (2012). <https://doi.org/10.1103/PhysRevLett.108.264504>
- Huang, H., Zhang, F., Callahan, P., Ayoub, J.: Granular fingering in fluid injection into dense granular media in a hele-shaw cell. *Phys. Rev. Lett.* **108**, 258001 (2012). <https://doi.org/10.1103/PhysRevLett.108.258001>
- Jain, A.K., Juanes, R.: Preferential Mode of gas invasion in sediments: grain-scale mechanistic model of coupled multiphase fluid flow and sediment mechanics. *J. Geophys. Res. Solid Earth* **114**, 1–19 (2009). <https://doi.org/10.1029/2008JB006002>

- Jeon, M.-K., Kim, S., Zadeh, A.H., Kwon, T.-H.: Study on viscous fluid flow in disordered-deformable porous media using hydro-mechanically coupled pore-network modeling. *Transp. Porous Med.* **133**, 207–227 (2020a). <https://doi.org/10.1007/s11242-020-01419-8>
- Jeon, M.-K., Zadeh, A.H., Kim, S., Kwon, T.-H.: Fluid-driven mechanical responses of deformable porous media during two-phase flows: Hele-Shaw experiments and hydro-mechanically coupled pore network modeling. In: *E3S Web of Conferences*, p. 08009. EDP Sciences (2020b)
- Johnson, K.L.: *Contact Mechanics*. Cambridge University Press, Cambridge (1987)
- Kueper, B.H., Abbott, W., Farquhar, G.: Experimental observations of multiphase flow in heterogeneous porous media. *J. Contam. Hydrol.* **5**, 83–95 (1989). [https://doi.org/10.1016/0169-7722\(89\)90007-7](https://doi.org/10.1016/0169-7722(89)90007-7)
- Lee, S., Lee, J., Le Mestre, R., Xu, F., MacMinn, C.W.: Migration, trapping, and venting of gas in a soft granular material. *Phys. Rev. Fluids* **5**, 084307 (2020). <https://doi.org/10.1103/PhysRevFluids.5.084307>
- Lenormand, R., Touboul, E., Zarcone, C.: Numerical models and experiments on immiscible displacements in porous media. *J. Fluid Mech.* **189**, 165–187 (1988)
- Li, J., McDougall, S.R., Sorbie, K.S.: Dynamic pore-scale network model (PNM) of water imbibition in porous media. *Adv. Water Resour.* **107**, 191–211 (2017)
- MacMinn, C.W., Dufresne, E.R., Wettlaufer, J.S.: Fluid-driven deformation of a soft granular material. *Phys. Rev. X* **5**, 011020 (2015)
- Mahabadi, N., Jang, J.: The impact of fluid flow on force chains in granular media. *Appl. Phys. Lett.* **110**, 041907 (2017)
- Meng, Y., Primkulov, B.K., Yang, Z., Kwok, C.Y., Juanes, R.: Jamming transition and emergence of fracturing in wet granular media. *Phys. Rev. Res.* **2**, 022012 (2020). <https://doi.org/10.1103/PhysRevResearch.2.022012>
- Monfared, K.A., Rothenburg, L.: Poroelasticity during fluid injection in confined geological reservoirs: incorporating effects of seal-rock stiffness. *SPE J.* **22**, 184–197 (2016). <https://doi.org/10.2118/181744-PA>
- Rocco, S., Woods, A.W., Harrington, J., Norris, S.: An experimental model of episodic gas release through fracture of fluid confined within a pressurized elastic reservoir. *Geophys. Res. Lett.* **44**, 751–759 (2017). <https://doi.org/10.1002/2016GL071546>
- Sandnes, B., Flekkøy, E.G., Knudsen, H.A., Måløy, K.J., See, H.: Patterns and flow in frictional fluid dynamics. *Nat. Commun.* **2**, 288 (2011)
- Shin, H., Santamarina, J.C.: Fluid-driven fractures in uncemented sediments: underlying particle-level processes. *Earth Planet. Sci. Lett.* **299**, 180–189 (2010). <https://doi.org/10.1016/j.epsl.2010.08.033>
- Støverud, K.H., Darcis, M., Helmig, R., Hassanzadeh, S.M.: Modeling concentration distribution and deformation during convection-enhanced drug delivery into brain tissue. *Transp. Porous Med.* **92**, 119–143 (2012). <https://doi.org/10.1007/s11242-011-9894-7>
- Sun, Z., Santamarina, J.C.: Grain-displacive gas migration in fine-grained sediments. *J. Geophys. Res. Solid Earth* **124**, 2274–2285 (2019). <https://doi.org/10.1029/2018JB016394>
- Wang, Y., Zhang, C., Wei, N., Oostrom, M., Wietsma, T.W., Li, X., Bonneville, A.: Experimental study of crossover from capillary to viscous fingering for supercritical CO<sub>2</sub>–water displacement in a homogeneous pore network. *Environ. Sci. Technol.* **47**, 212–218 (2013). <https://doi.org/10.1021/es3014503>
- Zadeh, A.H., Jeon, M.-K., Kwon, T.-H., Kim, S.: Pore-scale experimental study on fluid injection into two-dimensional deformable porous media. *Int. J. Multiphase Flow* **160**, 104376 (2023). <https://doi.org/10.1016/j.ijmultiphaseflow.2022.104376>
- Zhang, C., Oostrom, M., Wietsma, T.W., Grate, J.W., Warner, M.G.: Influence of viscous and capillary forces on immiscible fluid displacement: pore-scale experimental study in a water-wet micromodel demonstrating viscous and capillary fingering. *Energy Fuels* **25**, 3493–3505 (2011). <https://doi.org/10.1021/ef101732k>
- Zheng, X., Mahabadi, N., Yun, T.S., Jang, J.: Effect of capillary and viscous force on CO<sub>2</sub> saturation and invasion pattern in the microfluidic chip. *J. Geophys. Res. Solid Earth* **122**, 1634–1647 (2017). <https://doi.org/10.1002/2016JB013908>

**Publisher's Note** Springer Nature remains neutral with regard to jurisdictional claims in published maps and institutional affiliations.

## Authors and Affiliations

Min-Kyung Jeon<sup>1</sup>  · Seunghee Kim<sup>2</sup>  · Tae-Hyuk Kwon<sup>3</sup> 

✉ Tae-Hyuk Kwon  
t.kwon@kaist.ac.kr

Min-Kyung Jeon  
mkjeon@kigam.re.kr

Seunghee Kim  
seunghee.kim@unl.edu

<sup>1</sup> CO2 Geological Storage Research Center, Korea Institute of Geoscience and Mineral Resources (KIGAM), Daejeon, Korea

<sup>2</sup> Department of Civil and Environmental Engineering, University of Nebraska-Lincoln, Omaha, NE, USA

<sup>3</sup> Department of Civil and Environmental Engineering, Korea Advanced Institute of Science and Technology (KAIST), Daejeon, Korea